

Finite spatial-grid effects in energy-conserving particle-in-cell algorithms

D. C. Barnes^{a,*}, L. Chacón^b

^a*Coronado Consulting, Lamy, NM 87540*

^b*Los Alamos National Laboratory, Los Alamos, NM 87545*

Abstract

Finite-grid (or aliasing) instabilities are pervasive in particle-in-cell (PIC) plasma simulation algorithms, and force the modeler to resolve the smallest (Debye) length scale in the problem regardless of dynamical relevance. These instabilities originate in the aliasing of interpolation errors between mesh quantities and particles (which live in the space-time continuum). Recently, strictly energy-conserving PIC (EC-PIC) algorithms have been developed that promise enhanced robustness against aliasing instabilities. In this study, we confirm by analysis that EC-PIC is stable against aliasing instabilities for stationary plasmas. For drifting plasmas, we demonstrate by analysis and numerical experiments that, while EC-PIC algorithms are not free from these instabilities in principle, they feature a benign stability threshold for finite-temperature plasmas that make them usable in practice for a large class of problems (featuring ambipolarity and realistic ion-electron mass ratios) without the need to resolve Debye lengths spatially. We also demonstrate that this threshold is absent for the popular momentum-conserving PIC algorithms, which are therefore unstable for both drifting and stationary plasmas.

1. Introduction

The Particle-In-Cell (PIC) method has proven to be one of the most useful tools for simulation of plasmas. In addition to its intuitive feel of reproducing collective behavior by following individual numerical markers, it lends itself easily to situations in which complex boundary conditions, and/or interaction between several species (such as neutrals with ionization and related physics) must be accommodated. Along with these advantages, traditional PIC methods manifest some quite stringent limitations. Modern algorithmic improvements have worked toward eliminating or controlling these limitations. One such limitation is associated with the aliasing or finite-grid instability, first studied systematically by Langdon [1] and later by Birdsall and Maron [2]. The classic book by Birdsall and Langdon [3] contains a useful introduction to this subject in Chapter 8, and our present work follows closely this approach.

There has been renewed interest on the subject of aliasing instabilities in PIC methods. A recent discussion from a theoretical and empirical viewpoint [4] shows that this instability is ubiquitous in PIC methods. The study in Ref. [5] derives dispersion relations (verified by numerical experiments) for the aliasing instabilities in a classical electromagnetic explicit algorithm, with momentum-conserving deposition. The importance of the lack of spectral fidelity of the particle representation in aliasing instabilities in explicit, momentum-conserving PIC is explored in Ref. [6].

The motivation for this study is the apparent lack of aliasing instabilities in recently proposed fully implicit, energy-conserving PIC algorithms [7, 8, 9, 10, 11], which take advantage of modern iterative solvers, e.g. Jacobian-free Newton-Krylov (JFNK) methods [12] or Picard-accelerated methods [13]. This

*Corresponding author

Email address: coronadocon@msn.com (D. C. Barnes)

empirical observation has been reported by all groups investigating this approach. Hence the situation is unclear, as on the one hand, theory clearly indicates the possibility of instability for cold, drifting beams [14], and on the other hand, it is difficult to observe any difficulties associated with these instabilities in practical applications.

In usual PIC algorithms, the Debye length must equal or exceed the cell size for stability against the aliasing instability, even though the physics often does not depend on Debye-length physics. For example, dense plasmas often are described well by the quasi-neutral approximation in most of the domain, so that fidelity to the relevant physics could be obtained with much larger linear cell size. The impact of using a cell size compatible with the physics requirement vs. one of the Debye length is enormous in higher dimensions, and can easily lead to a one million times reduction of computational expense in both time and memory. Thus, there is a strong motivation for better understanding of this subject.

The approach of this study is to understand by numerical analysis and corresponding numerical experiments the effect of finite spatial grid effects for both cold and thermal drifting populations on the stability of energy-conserving PIC (EC-PIC) algorithms. Given that finite-grid instabilities are electrostatic in nature, we focus the discussion on electrostatic EC-PIC algorithms (such as the one in Ref. [7], which is also implicit and charge conserving, and we term here CCB). Given the focus on finite-grid instabilities, we consider the $\Delta t \rightarrow 0$ limit of CCB. The assumption of zero time step means that any conclusions can be applied to an energy-conserving PIC method with any time-stepping scheme, and this feature is discussed in our conclusions.

Energy-conserving PIC methods were introduced by Lewis and others around 1970 [15] and shortly afterward were examined theoretically and empirically for aliasing instabilities [14]. This early work indicated that there was no particular distinction of EC-PIC approaches compared with the established momentum-conserving methods, as far as avoidance of aliasing instabilities. It was shown that: 1) energy is not particularly well-conserved by the early, time-explicit implementations; 2) cold-drifting beams were unstable with comparable linear growth rates and comparable nonlinear consequences; 3) lack of momentum conservation allowed conversion of drift energy to thermal energy *via* the aliasing instability. While some hopeful signs that aliasing instabilities might be avoided in some applications,¹ the situation seemed not sufficiently hopeful to advance EC-PIC approaches instead of momentum-conserving ones.

In the last nearly half century, computing has advanced beyond all expectations, and this explosion in capability now allows detailed examination of a sufficiently large parameter space. Quite different conclusions can be drawn from this enlarged perspective. We find a new stability regime for drifting thermal (Maxwellian) electrons, which is relevant for modern applications with realistic mass ratios. In fact, this regime may be (and has been) exploited in applying PIC to dense, quasi-neutral simulations, completely avoiding aliasing instabilities with cell sizes up to more than 100 times plasma Debye length. We follow the established approach to derive and solve (usual) dispersion relations (DRs) associated with spatial grid effects and to compare growth-rate predictions with numerical experiments. Our extended survey of these results leads to new and hopeful conclusions about aliasing in energy-conserving methods and explains the apparent success of these methods in avoiding Debye length restrictions. In fact, while EC-PIC does not suffer from aliasing instabilities in stationary thermal populations (as reported for instance in Ref. [16]), aliasing instabilities are present in EC-PIC algorithms for cold-beam drifting populations. While the combination of smoother (continuously differentiable) charge-conserving scatter and binomial smoothing (as proposed in the original CCB algorithm [7]) is useful in significantly reducing growth rates of linearly unstable cold-beam aliasing modes, and in ameliorating the Debye-length resolution requirement for stability, these are not required to access a previously unidentified stability region, namely, EC-PIC algorithms are

¹See Ref. [3], p. 177 comment in caption of Fig. 8-12b concerning the stability threshold on the drift velocity for energy-conserving methods.

stable below a critical Mach number (defined as the ratio of the electron drift to thermal velocities) of $\mathcal{O}(1)$. The implication is that, as we discuss, EC-PIC algorithms may not require resolution of the Debye length in ambipolar plasma systems when using realistic ion-electron mass ratios, and aliasing instability may be easily avoided in practical applications.

The rest of this paper is organized as follows. Section 2 derives the relevant dispersion relations for the numerical scheme for cold (zero temperature) and warm beams. The numerical analysis of the dispersion relations to find unstable roots is performed in Sec. 3. Numerical experiments verifying key results from the analysis and illustrating the main conclusions of this paper are provided in Sec. 4. Finally, we conclude in Sec. 5.

2. Dispersion relations

In this section, we derive the required dispersion relations for cold and warm beam cases, including binomial smoothing and all effects of a discrete spatial grid (but for the limit of zero time step).

2.1. Equivalent electrostatic formulation

An exact charge-conserving scheme such as CCB is mathematically equivalent to a formulation in terms of the electrostatic potential ϕ . Indeed charge conservation means that there exists a density shape function s which is related to the current/electric field shape function \hat{s} by finite differences to round-off accuracy. Thus, the edge-centered \hat{s} and the vertex-centered s satisfy [17]

$$s_i(x^1) - s_i(x^0) = -(x^1 - x^0) \frac{\hat{s}_{i+1/2}(x^{1/2}) - \hat{s}_{i-1/2}(x^{1/2})}{\Delta} \quad (1)$$

where Δ is the mesh spacing (assumed uniform here).

Multiplying this by the vertex-centered potential ϕ_i and summing over i , we obtain, after re-arranging the sum on the right

$$-\frac{\phi(x^1) - \phi(x^0)}{x^1 - x^0} = \sum_i \hat{s}_{i+1/2}(x^{1/2}) \left(-\frac{\phi_{i+1} - \phi_i}{\Delta} \right) \quad (2)$$

where we have defined the interpolation of the potential as $\phi(x) = \sum_i s_i(x) \phi_i$. The right hand side of Eq. (2) is just the energy-conserving interpolation of the edge-centered electric field used in CCB, where the electric field is defined as $E_{i+1/2} = -(\phi_{i+1} - \phi_i)/\Delta$.

2.2. Cold drifting beam

The results of the previous sub-section shows that the CCB orbit equations may also be written as

$$\begin{aligned} x^{n+1} - x^n &= \Delta t v^{n+1/2} \\ v^{n+1} - v^n &= -\frac{q_p \Delta t}{m_p} \frac{\phi^{n+1/2}(x^{n+1}) - \phi^{n+1/2}(x^n)}{x^{n+1} - x^n} \end{aligned} \quad (3)$$

where $\phi(x) = \sum_i s(x - x_i) \phi_i$ is the potential interpolated from the mesh, and $s(x - x_i)$ is the density shape function. It is obvious that, in the limit of zero time step, this yields:

$$\begin{aligned} \dot{x} &= v \\ \dot{v} &= -\frac{q_p}{m_p} \partial_x \phi(x) \end{aligned}$$

The consistent charge deposition associated with this scheme is

$$\rho_i = \frac{1}{\Delta} \sum q_p s(x - x_i), \quad (4)$$

with Δ the grid spacing. In the small-amplitude limit, the particle positions x are displaced by δx and the perturbed charge density reads:

$$\rho_i = \frac{1}{\Delta} \sum_p q_p \delta x \partial_x s(x - x_i). \quad (5)$$

In this way, the only spline which enters the formulation is s , with (infinite) Fourier transform $S(k)$. Choosing s to be the m -th order B-spline, we have:

$$S(k) = \left[\frac{\sin(k\Delta/2)}{k\Delta/2} \right]^{m+1}. \quad (6)$$

Following the aliasing formulation given in Birdsall and Langdon [3], we find the DR for a beam with drift velocity U as:

$$D = 1 - \frac{\omega_p^2}{K^2} \sum_q \frac{k_q^2 [S(k_q)]^2}{(\omega - k_q v)^2} = 0, \quad (7)$$

where $k_q = k + 2\pi q/\Delta$ is the alias wave number, and

$$K^2 = \left[k \frac{\sin(k\Delta/2)}{k\Delta/2} \right]^2 \quad (8)$$

is the negative of transform of the finite-difference Laplacian. Equation 7 is identical to the one found for Lewis' energy-conserving method [15] in Sec. 8-11 of Ref. [3]. Using Eqs. 6 and 8, we find:

$$D = 1 - \omega_p^2 [\sin(k\Delta/2)]^{2m} \cos^4(k\Delta/2) \sum_q \frac{1}{(k_q \Delta/2)^{2m} (\omega - k_q U)^2} = 0, \quad (9)$$

where the $\cos^4(k\Delta/2)$ factor is present when a binomial $(1, 2, 1)/4$ filter is applied on the mesh twice per cycle, as originally proposed in CCB [7].

We introduce the normalized variables $\kappa = k\Delta$, $u = U/\omega_p \Delta$ and $\bar{\omega} = \omega/\omega_p$ to re-write Eq. 9 as:

$$D = 1 - [\sin(\kappa/2)]^{2m} \cos^4(\kappa/2) \sum_q \frac{1}{(\kappa/2 + q\pi)^{2m} (\bar{\omega} - \kappa u - 2q\pi u)^2} = 0. \quad (10)$$

The case $m = 0$ with no digital filter, while unphysical (one cannot interpolate ϕ with nearest-grid-point formulae, as they cannot capture electric fields correctly), is particularly simple, because of the identity

$$(\pi \csc \pi z)^2 = \sum_q \frac{1}{(z - q)^2}.$$

Thus, for this case, the dispersion relation becomes:

$$1 = \frac{(2u)^{-2}}{\sin^2 \left[(2u)^{-1} (\bar{\omega} - \kappa u) \right]} \quad (11)$$

It is easy to see from Eq. 11 that there is stability for $u > 1/2$ and instability otherwise (simply using the fact that $|\sin(x)| \leq 1$ for real x). This suggests that energy conserving PIC may be unstable to beam modes when the drift velocity is small enough, just as in explicit PIC methods. We will consider the realistic case of $m > 0$ numerically later in this study.

2.3. Warm beam

The previous results can be extended to the case of a drifting Maxwellian,

$$\bar{f} = \frac{\bar{n} e^{-m(v-U)^2/2T}}{\sqrt{2\pi T/m}}. \quad (12)$$

The solution for the dispersion relation can be obtained by convolving the cold-beam solution Eq. 7 with the equilibrium distribution function \bar{f} , to find:

$$1 - \frac{\omega_p^2}{K^2} \sum_q k_q^2 [S(k_q)]^2 \int_{-\infty}^{\infty} dv \frac{e^{-v^2/2v_T^2}}{\sqrt{2\pi}v_T (\omega - k_q v)^2} = 0, \quad (13)$$

where $v_T^2 = T/m$. There results:

$$1 + 4 \frac{[\sin(\kappa/2)]^{2m}}{\lambda^2} \sum_q \frac{1 + \Omega_q Z(\Omega_q)}{(\kappa/2 + \pi q)^{2(m+1)}} = 0, \quad (14)$$

where the dimensionless argument of the Fried-Conte function Z is:

$$\Omega_q = \frac{1}{\sqrt{2}\lambda} \left(\frac{\bar{\omega}}{\kappa + 2\pi q} - u \right) \text{sign}(\kappa + 2\pi q), \quad (15)$$

with $\lambda = \lambda_D/\Delta$. The sign function in Eq. 15 is required so that the imaginary part of ω is treated properly in the Z functions.

As in the cold-beam case, the effects of the $(1, 2, 1)/4$ binomial mesh filter can be readily included with an additional $\cos^4(k\Delta/2)$ factor, and the final dispersion relation reads:

$$1 + 4 \frac{[\sin(\kappa/2)]^{2m} [\cos(\kappa/2)]^4}{\lambda^2} \sum_q \frac{1 + \Omega_q Z(\Omega_q)}{(\kappa/2 + \pi q)^{2(m+1)}} = 0. \quad (16)$$

We show next that Eq. 16 reduces to the cold-beam result when λ goes to zero. In this case, the arguments of the Z functions become large and we use the asymptotic limits

$$Z(\zeta) \sim -\frac{1}{\zeta} \left(1 + \frac{1}{2\zeta^2} + \dots \right) + \mathcal{O}\left(e^{-\zeta^2/2}\right) \quad (17)$$

The last (exponential) term will not be important because we focus here only on growing modes for which this term is exponentially small. Substituting this into Eq. 16 we find, to leading order:

$$1 - 4 \frac{[\sin(\kappa/2)]^{2m} [\cos(\kappa/2)]^4}{\lambda^2} \sum_q \frac{1/2\Omega_q^2}{(\kappa/2 + \pi q)^{2(m+1)}} = 0, \quad (18)$$

which, when substituting Eq. 15, gives the cold-beam dispersion relation of Eq. 10.

3. Numerical analysis

The dispersion relation is studied by specifying the dimensionless parameters λ, u along with m and an artificial limit Q on the sum on q . The normalized wave number κ is scanned over the first Brillouin zone from $[-\pi, \pi]$. In order to assure, as completely as possible, that all relevant roots are located, we proceed in a systematic manner. A ‘‘box’’ in the complex plane is defined as shown in Fig. 1. The upper limit of the box is chosen larger than any root (roots cannot have a growth rate more than several ω_p , so normalized $\bar{\omega}$

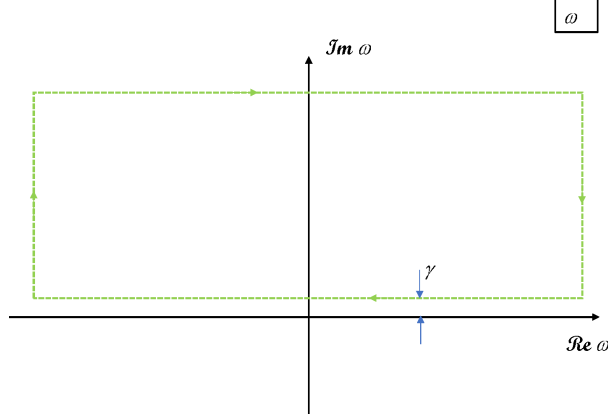


Figure 1: Integration box for finding unstable complex roots.

is limited to a few). Similarly, the left and right limits are chosen so that all real frequencies of interest fall within the box. The lower limit γ is scanned from some small value (defined as that for which the numerical evaluation of required functions is well behaved) in small steps upward. At each step, the contour integral

$$I(\gamma) = \oint \frac{dz}{\varepsilon} \quad (19)$$

is evaluated, where $\varepsilon = 0$ is the dispersion relation of interest. The lower limit is then raised in small steps, I is evaluated at each step using the LSODE ODE package [18] with adaptive, higher-order method, and its absolute value is examined. When γ exceeds the growth rate of the fastest-growing mode, there are no singularities of the integrand located in the resulting box, and the value of I drops to near zero. The fastest-growing mode is then determined to have a growth rate between the value of γ which gives a significant value of I and that which gives a near zero value.

The results of this procedure have been checked by an alternative solution of the cold-beam dispersion relation of Sec. 2.2. This may be formed into the problem of finding the zeros of a polynomial of moderate degree (typically 28 to 40). Since such a problem has a known number of roots, we use previously described methods [19] to find all zeros, along with error estimates of the location of each root. These approximations are then used as starting points for the secant method to find zeros of the DR as written in Eq. 10. Convergence of this procedure assures that no spurious roots are introduced by conversion into a polynomial equation.

To recast the DR of Eq. 10 into the standard problem of finding the zeros of a polynomial, we clear denominators

$$\prod_q (\bar{\omega} - \kappa u - 2q\pi u)^2 - [\sin(\kappa/2)]^{2m} \cos^4(\kappa/2) \sum_q \frac{1}{(\kappa/2 + q\pi)^{2m}} \prod_{q' \neq q} (\bar{\omega} - \kappa u - 2q'\pi u)^2 = 0 \quad (20)$$

resulting in a polynomial equation of degree $2(2Q - 1)$. The Culham Laboratory-originated Fortran routine PA16AD, based on the work of Bini [19], is used to locate the roots of this polynomial equation. Results agree with the box method described previously, and show instability for a large range of drift velocity and for every method considered here.

A comparison of the growth rate for different choices of B-spline order m and filtering is shown in Fig. 2, where the maximum (over u) growth rate is plotted vs. κ for the cases $m = 1$ (linear spline) no binomial filter, $m = 1$ with binomial filter, $m = 2$ (quadratic spline) no binomial filter, and $m = 2$ with binomial filter. As can be seen, it is possible to reduce the linear growth rate by more than 5 times by use of smoother particle shape and binomial filtering, with the combination of both providing the most reduction.

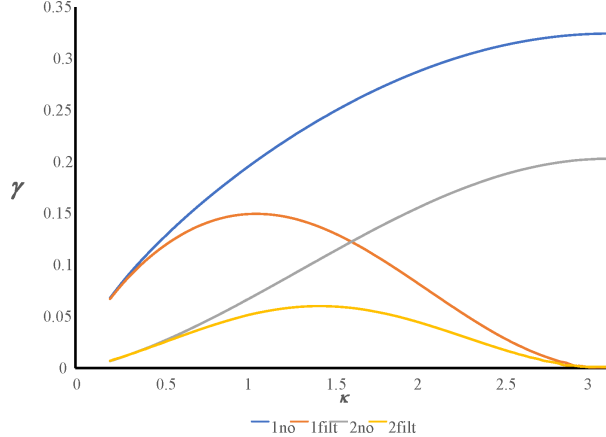


Figure 2: Cold-beam growth rate variation with wavenumber for four choices of shape function ($m = 1, 2$) and filtering (with and without filtering), as follows: yellow ($m = 2$, with filtering), gray ($m = 2$, without filtering), red ($m = 1$, with filtering), and blue ($m = 1$, without filtering).

A more comprehensive picture of the cold-beam alias modes is provided by Fig. 3, where contours of growth rate vs. both u and κ are displayed for each method. As can be seen the growth rates are significant (up to 32% of ω_p) and ubiquitous, as pointed out in numerous places in the literature. The “ridges” appearing in these contours result from multiple branches of the dispersion relation solutions. Figure 4 shows all roots (obtained by the polynomial root finder method) vs. u for a slice along a fixed $\kappa = 0.497$ of the case of Fig. 3 (d). The two prominent ridges near $u = 0.45$ and $u = 0.7$ are associated with branches of roots along which growth rates peak rapidly and then the branch terminates [such behavior may be expected from the multiple resonant denominators of Eq. (10)].

3.1. Warm-beam analysis

The effect of introducing a small beam thermal spread is examined next by finding roots of Eq. 14 as previously described. Figure 5 shows the results of adding a beam temperature to the previous results. The figures depict the growth rate as a function of Mach number (defined in normalized units as $M_{\#} = u/\lambda$) and drift velocity u . As can be seen, unstable modes exist only for a drift velocity exceeding a given Mach number, which is essentially 1.0 for the various cases. While the maximum growth rate is quite strongly dependent on the particulars of the method, the stability limits are largely independent of these.

These results for the energy-conserving formulation may be compared with those for the usual momentum-conserving scheme [3] employed in many PIC implementations. Figure 6 shows the same scan presented in Fig. 5, but repeated for the momentum-conserving methods. The stable region at low Mach is now replaced by the familiar cell-size to Debye length ratio stability constraint known for the aliasing stability of momentum-conserving PIC.

With the improved viewpoint provided by these wide-ranging scans, we find a new result that the stability of EC-PIC for a warm-drifting beam distribution is qualitatively different from that of usual momentum-conserving PIC algorithms, which typically require cell sizes limited to a small multiple of Debye length (Fig. 6). Namely, for energy-conserving PIC, a new stability region appears at low to modest Mach numbers that is independent of cell size. This result implies that, at worst, finite-grid instabilities in energy-conserving PIC saturate when the thermal spread of the beam becomes comparable to the drift velocity. However, more importantly and as will be discussed subsequently, this property allows the application of the algorithm to a wide range of interesting ambipolar plasmas without interference from aliasing instabilities in practice.

It is also instructive to plot the stability diagrams for EC-PIC in terms of the normalized Debye length λ and drift velocity u (Fig. 7), to contrast against similar diagrams for the momentum-conserving PIC

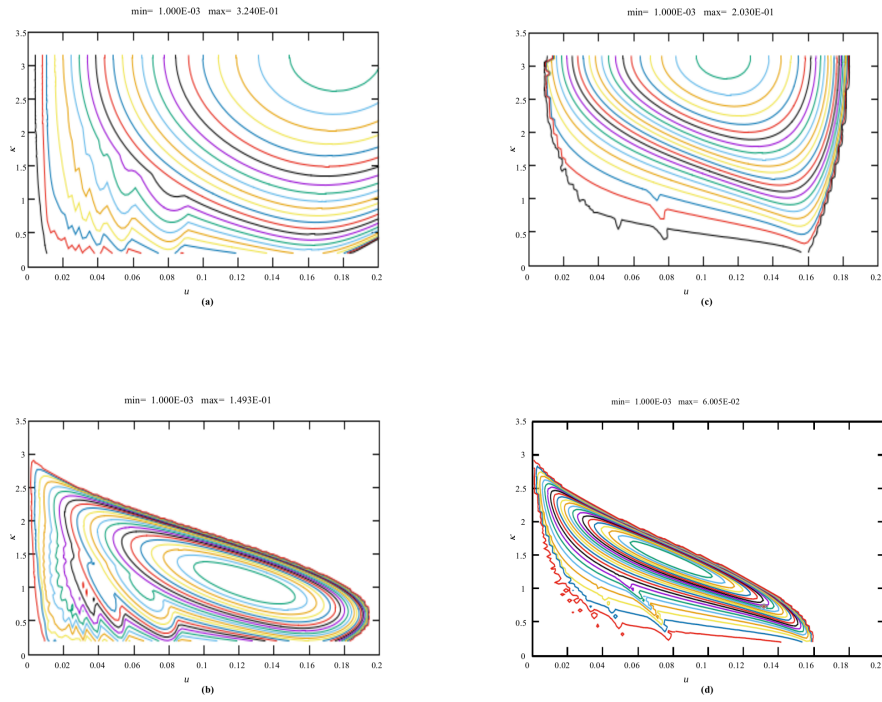


Figure 3: Contours of cold-beam growth rate vs. u and κ for four cases: (a) $m = 1$ (linear spline) no filter; (b) $m = 2$ (quadratic spline) no filter; (c) $m = 1$ with filter; (d) $m = 2$ with filter.

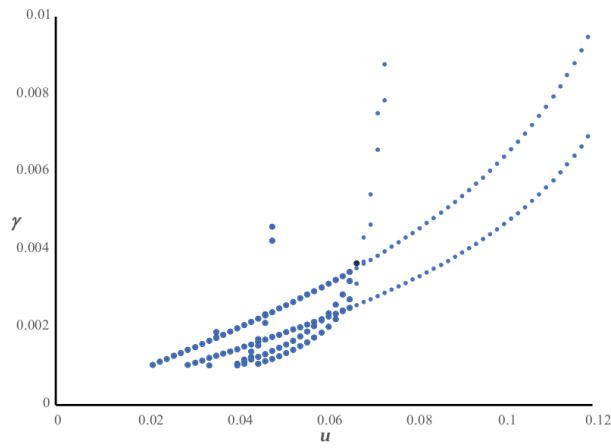


Figure 4: Growth rate vs. u for all unstable modes for $\kappa = 0.497$ showing the existence of ridges at which unstable modes become suddenly stable.

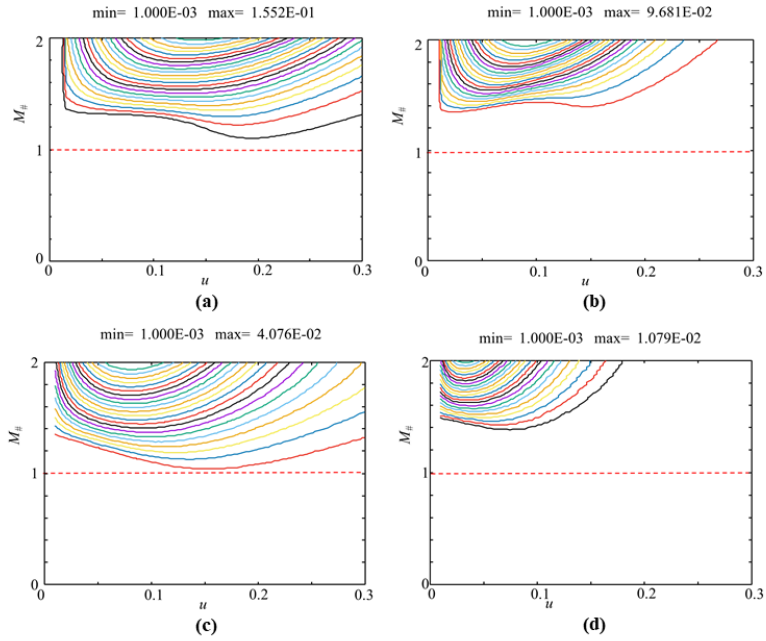


Figure 5: Contours of warm-beam growth rate vs. u and Mach number $M_{\#}$ for four cases: (a) $m = 1$ (linear spline) without filter; (b) $m = 2$ (quadratic spline) without filter; (c) $m = 1$ with filter; (d) $m = 2$ with filter. Dashed horizontal line indicates Mach 1.0 to gauge stability limit.

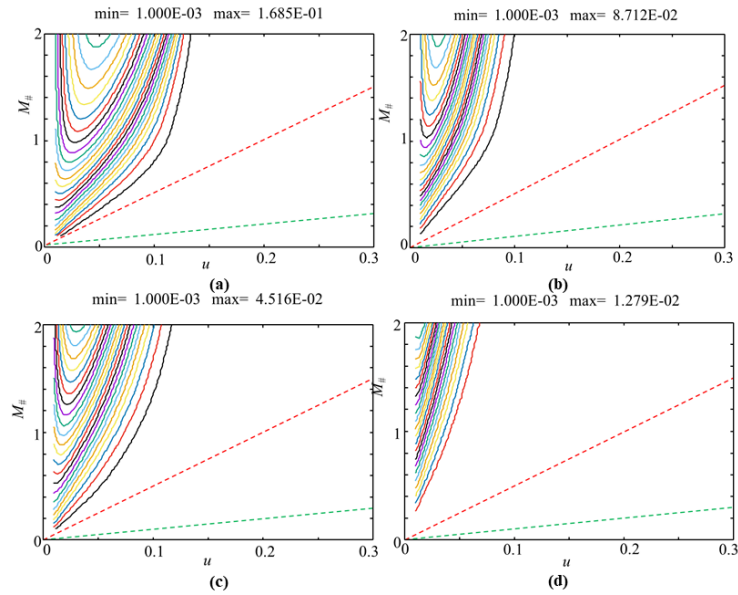


Figure 6: Same plots as those of Fig. 5 for the momentum-conserving method. Dashed lines indicate $\Delta/\lambda_D = 1/\lambda$ of 1 (green) and 5 (red).

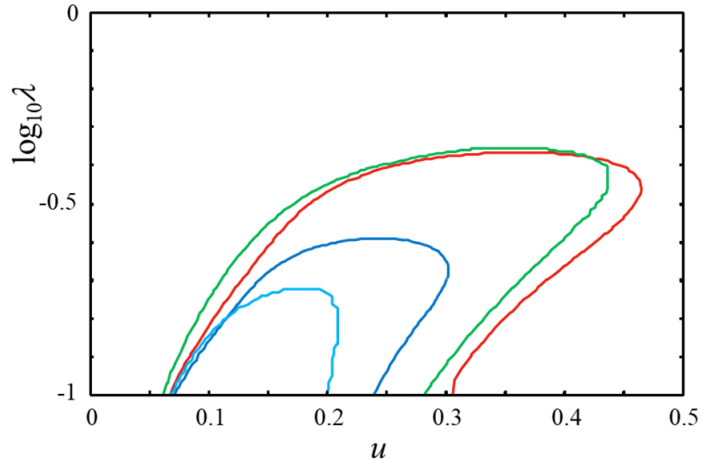


Figure 7: Marginal contours in $\log_{10}\lambda, u$ space for four cases: red – linear spline, no filter; green – linear spline, filter; blue – quadratic spline, no filter; cyan – quadratic spline, filter

algorithms. From this figure, it is apparent that absolute stability is attained for arbitrary u above a threshold in $\lambda = \lambda_D/\Delta$, i.e., when the Debye length is sufficiently resolved. The threshold, however, is strongly dependent on the interpolation order m and the use of filtering. While the impact of filtering for first-order splines is minimal, it is significant for higher-order interpolations. For first-order interpolation, the stability limit is $\Delta \lesssim 4\lambda_D$. For second-order splines, absolute stability with smoothing is achieved for $\Delta \lesssim 8\lambda_D$, which is a factor of 2 larger than the first-order-spline stability limit (which would result in efficiency gains of $2^4 \sim 16$ in 3D+time just from the easing of spatial and temporal resolution requirements). For filtered third-order splines (not shown), the limit is $\Delta \lesssim 12\lambda_D$, resulting in potential efficiency gains vs. first-order interpolation of more than 1000. The impact of smoothing on the stability thresholds in u is also apparent from Fig. 7, with the unstable region shrinking significantly with both spline order and filtering.

4. Numerical experiments

We perform numerical simulations with the CCB algorithm ($m = 2$) with and without binomial smoothing, to confirm the validity of the previous linear theory analysis. Our simulation setup considers $\Delta = 1$ and $\omega_p = 1$, and therefore code units correspond to dimensionless units in the previous section. We consider a single-species simulation with 256 particles per cell, and 128 cells (and therefore the domain length is $L = 128$). Both cold-beam and warm-beam simulations are initialized with random particle positioning in the simulation coordinate (to perturb all wavenumbers). Growth rates are obtained by Fourier-decomposing the signal, and searching for the fastest growing mode. Since growing aliasing modes are oscillatory, and saturation amplitudes for some of these modes are small, for some of these measurements there is a limited growth time window to obtain growth rates, and therefore the growth rate measurements are only approximate.

4.1. Cold-beam results

We begin by verifying our cold-beam semi-analytical results with numerical experiments. The results are depicted in Fig. 8, where numerical growth rates are compared against analytical growth rates for the case of $m = 2$, with and without binomial smoothing. Agreement is excellent.

Figure 9 shows phase-space plots of initial and final phase-space solutions of a cold-beam simulation with $u = 0.1$, $m = 2$, with and without filtering ($t = 100$ for unfiltered, 1000 for filtered). Charge and energy

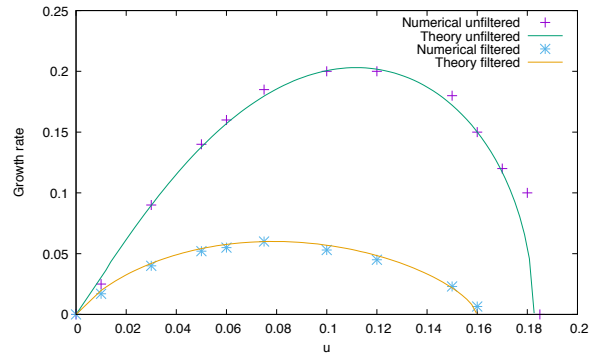


Figure 8: Growth rate comparison between the cold-beam theory and numerical experiment for $m = 2$, with and without filtering.

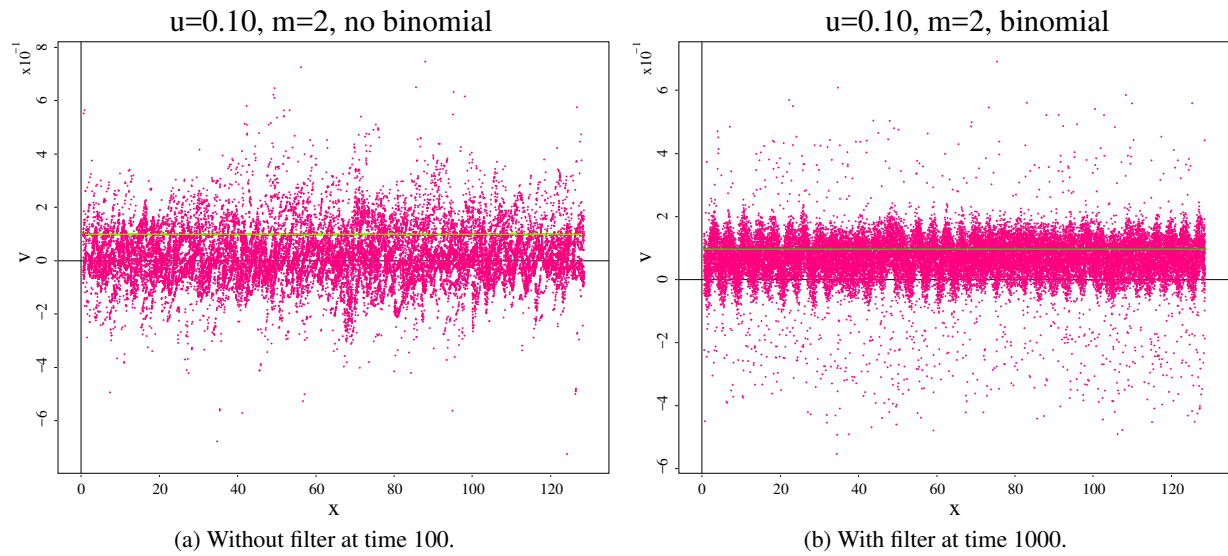


Figure 9: Nonlinearly saturated cold-beam phase-space plots of initial (green) and final (red) states for $u = 0.1$ and $m = 2$, with and without filtering.

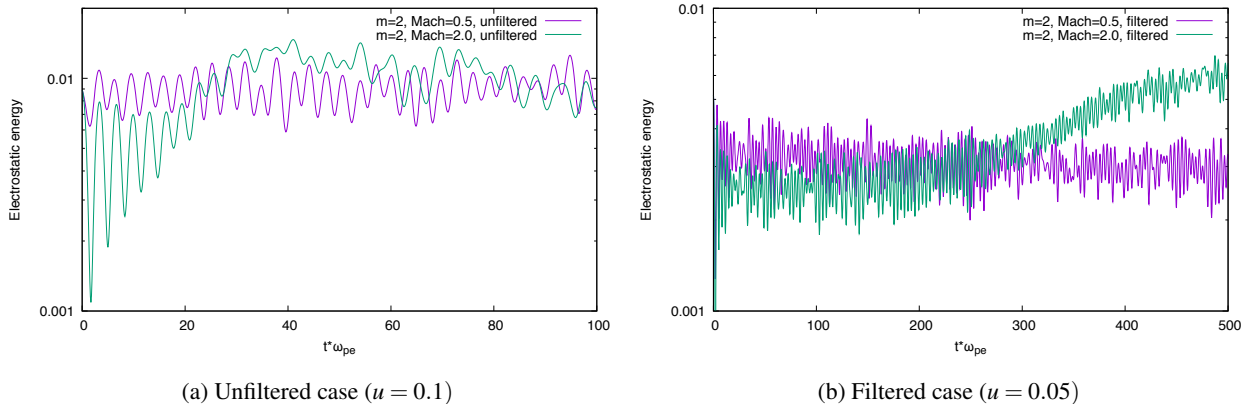


Figure 10: Warm beam numerical time histories for the electrostatic energy for $m = 2$, both filtered and unfiltered. The unfiltered case is more unstable, as evidenced by the much quicker saturation of the instability.

are conserved to round-off in both cases, and the instability has saturated nonlinearly by the end of the simulation. It can be clearly appreciated in both cases that the instability saturates when the thermal velocity of the beam becomes comparable to the initial drift velocity, which is consistent with the warm-beam linear theory above. However, the filtered simulation takes much longer to saturate, owing to the much smaller linear growth rates.

4.2. Warm-beam results

Next, we test the linear-theory predictions of Fig. 5 for the warm beam with CCB. We have run both filtered and unfiltered cases for $m = 2$, with normalized drift velocities chosen to maximize the growth rate ($u = 0.1$ for the unfiltered case, $u = 0.05$ for the filtered one). We have chosen two Mach numbers, $M_{\#} = 0.5$ (which should be stable for both cases), and $M_{\#} = 2$ (which should be unstable and with sufficiently large growth rates, but much more so for the unfiltered case). The results are presented in Fig. 10, which depicts time histories of the electrostatic energy, and confirm the linear-theory conclusions. A detailed Fourier analysis of the signal quantitatively confirms the growth rates computed by the linear theory analysis and reported in Fig. 5.

4.3. Plasma slab expansion into vacuum

We conclude our numerical exploration of the stability properties of EC-PIC with a 1D-1V plasma-expansion problem of a slab into vacuum. This problem has been chosen to exemplify the constraints that ambipolarity imposes on the electron Mach number, which leads to robust behavior against aliasing instabilities even when $\lambda \ll 1$. Our problem setup is as follows. Normalization of time and space is chosen as in the theoretical development presented earlier in this study. The plasma slab has initial charge density of unity, and is localized in a region of 25 Debye lengths at the right boundary. Ions and electrons are in thermal equilibrium and at rest, with the electron thermal velocity being unity (consistently with our normalization). We employ realistic ion-to-electron mass ratio, $m_i/m_e = 1846$. We simulate a domain of 500 Debye lengths, employing a 64-point variable mesh packed at the right boundary (with resolution of 1 Debye length), and extending out to the left boundary (with resolution of 20 Debye lengths). This mesh extension implies that the mesh is getting coarser as the plasma cools and expands, thereby stressing the algorithm more. The right boundary is reflecting, and the left boundary is open to vacuum. We use 5000 particles per cell for both ions and electrons. We use a second-order interpolation strategy ($m = 2$) without filtering. We run the problem to a final time of $T = 5000\omega_{pe}^{-1}$.

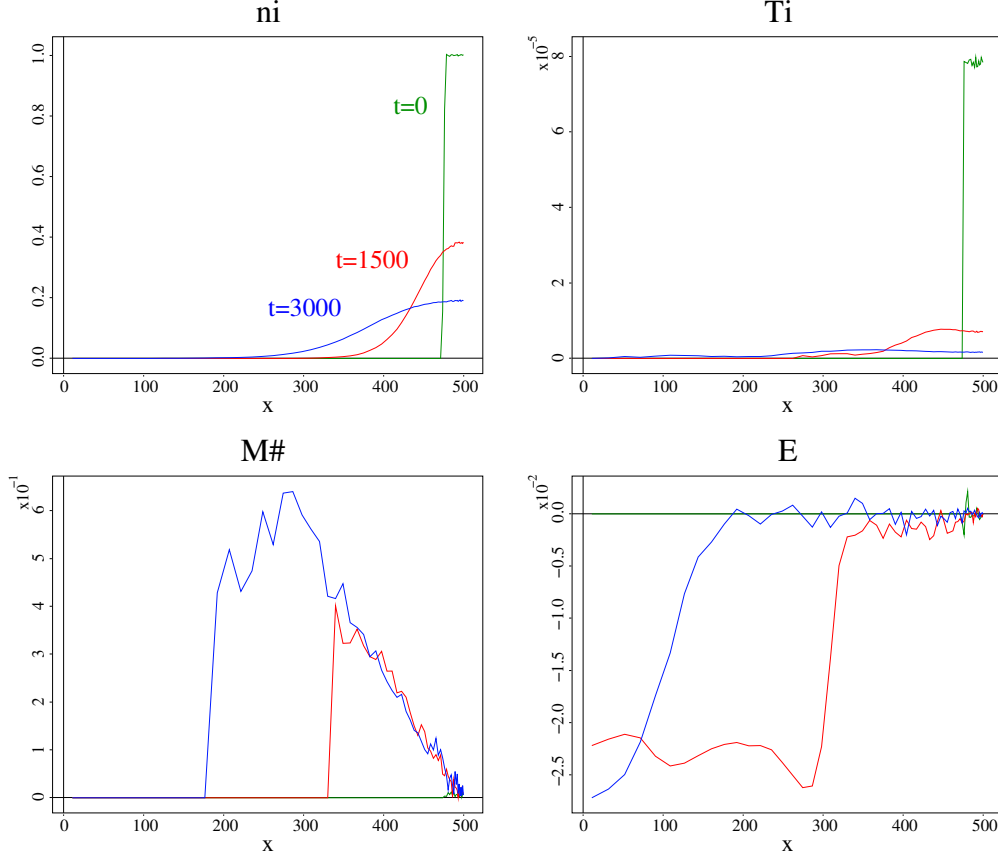


Figure 11: Spatial profiles of ion density n_i , ion temperature T_i , electron Mach number $M_\#$, and electric field E at time $t = 0$ (green), $t = 1500\omega_{pe}^{-1}$ (red), and $t = 3000\omega_{pe}^{-1}$ (blue), for the slab plasma expansion problem.

Profiles of ion density, temperature, electron Mach number, and electric field are depicted in Fig. 11, where it can be clearly appreciated the development of a finite ambipolar electric field as the slab expands due to faster electron motion. Owing to the presence of the ambipolar electric field, electrons are pulled back with the ions, and their Mach number is limited to about ~ 0.3 , below the stability limit of the algorithm. The Mach number diagnostic has been computed only when the ion plasma density is larger than 1% of the density at the right boundary at any given time, and when the electron thermal velocity is larger than 10^{-4} . This prevents pollution of the diagnostic with regions that are either very cold, or very rarefied, or both.

The strong stabilization of aliasing instabilities by the ambipolar electric field is demonstrated in Fig. 12, where time-history plots of $u-\lambda$ and $u-M_\#$ pairs for the plasma expansion problem are shown together with the stability boundary for the unfiltered $m = 2$ case presented in Fig. 11. The $u-\lambda$ (or $M_\#$) pairs are obtained as follows: for each time step, we compute the place where the maximum Mach number is located, and there we measure the normalized drift u and normalized Debye length λ . Different coloring of these pairs indicate time, according to the color legend on the right of each plot. The figure demonstrates that the expansion is concentrated in the stable region of the parameter space, giving a perfectly stable evolution despite λ values significantly smaller than 0.1.

5. Discussion and Conclusions

We have formulated the cold and warm beam electrostatic PIC dispersion relations including finite-grid effects in the limit of vanishing time step. Using improved numerical methods and considerable compute

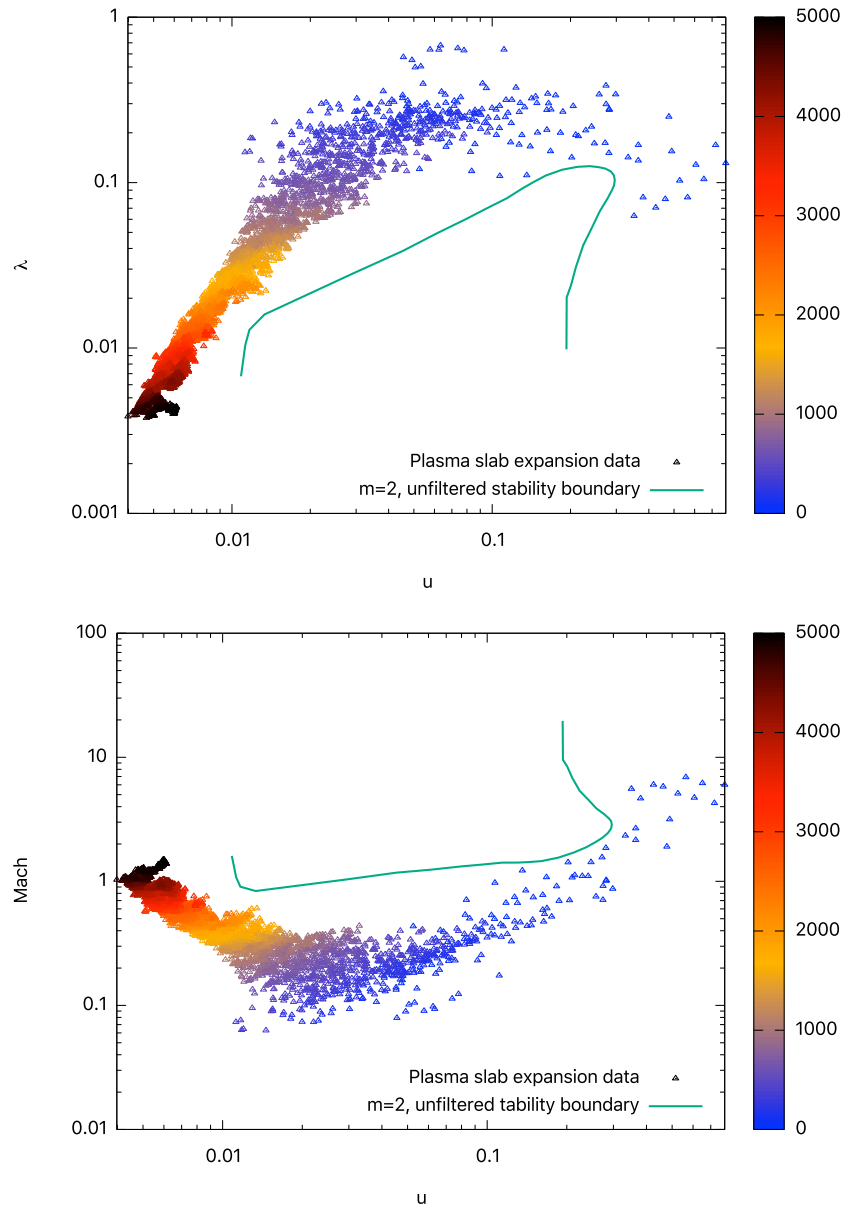


Figure 12: Demonstration of ambipolar stability in time of the unfiltered $m = 2$ algorithm using the plasma expansion problem. The green line represents the stability boundary given in Fig. 7.

time, we surveyed a wide range of dimensionless parameters for both energy- and momentum-conserving PIC methods. Results indicate a qualitatively different stability picture to that offered by previous studies. Momentum-conserving methods require a cell size a few times Debye length to avoid aliasing instabilities and associated rapid plasma heating. Energy-conserving methods, on the other hand, provide a new stability window at low to moderate Mach numbers. The stability threshold is around Mach 1.0, depending little on details of the particle shape and/or mesh filtering. These results have been confirmed qualitatively and quantitatively by comparison with PIC simulations using the modern methods of Ref. [7], and by the plasma slab expansion problem.

The implications of this new stability region are considerable for ambipolar plasmas (an important subset of applications, particularly of implicit PIC methods). In these plasmas, electrons remain coupled to the much more massive ions, which prevent them from reaching large drift speeds. As a result, electrons drift with ion-acoustic or smaller speeds, and the electron Mach number should remain well below the aliasing instability threshold found in this study. The Mach number threshold is found to be largely independent of the details of particle shape and mesh filtering strategies, indicating that it should be possible to capture this desirable operation in a variety of practical PIC methods (a confirmation of this result has been provided with the plasma slab expansion problem). However, it depends strongly on the ion-to-electron mass ratio, and therefore the effect may disappear if one uses unrealistically heavy electrons. We conclude that, once energy-conservation is built into the scheme, aliasing instabilities are effectively tamed for ambipolar plasmas, regardless of other algorithmic details.

For applications in which charge separation physics is critical (e.g., when driven by external means such as in laser-plasma interactions), aliasing instabilities may remain an issue in EC-PIC regardless of energy conservation, and judicious algorithmic choices in regards to smoothing and interpolation order may be critical to avoid their deleterious effects. In particular, we have shown that the combined use of higher-order interpolation and filtering may alleviate resolution requirements enough to speed up simulations by two to three orders of magnitude.

Finally, it is important to note that our analysis has been focused on the arbitrarily small timestep limit, and thus applies to both explicit and implicit (when using small timesteps) EC-PIC algorithms. However, as noted and demonstrated numerically in Ref. [20], large timesteps may significantly slow down aliasing instabilities in implicit PIC algorithms (after all, large timesteps can be looked at as a low-pass filter on allowable temporal modes). We leave the analysis of the large-timestep case for future work.

Acknowledgments

The authors would like to acknowledge useful conversations with G. Chen. LC was sponsored by the Office of Applied Scientific Computing Research (ASCR) of the US Department of Energy. This work was partially performed under the auspices of the National Nuclear Security Administration of the U.S. Department of Energy at Los Alamos National Laboratory, managed by LANS, LLC under contract DE-AC52-06NA25396.

References

- [1] A. B. Langdon, “Effects of the spatial grid in simulation plasmas,” *Journal of Computational Physics*, vol. 6, no. 2, pp. 247–267, 1970.
- [2] C. K. Birdsall and N. Maron, “Plasma self-heating and saturation due to numerical instabilities,” *Journal of Computational Physics*, vol. 36, no. 1, pp. 1–19, 1980.
- [3] C. Birdsall and A. Langdon, *Plasma Physics via Computer Simulation*. New York: McGraw-Hill, 1985.
- [4] J. Brackbill, “On energy and momentum conservation in particle-in-cell plasma simulation,” *Journal of Computational Physics*, vol. 317, pp. 405–427, 2016.
- [5] M. D. Meyers, C.-K. Huang, Y. Zeng, S. Yi, and B. J. Albright, “On the numerical dispersion of electromagnetic particle-in-cell code: Finite grid instability,” *Journal of Computational Physics*, vol. 297, pp. 565–583, 2015.
- [6] C.-K. Huang, Y. Zeng, Y. Wang, M. Meyers, S. Yi, and B. Albright, “Finite grid instability and spectral fidelity of the electrostatic particle-in-cell algorithm,” *Computer Physics Communications*, vol. 207, pp. 123–135, 2016.
- [7] G. Chen, L. Chacón, and D. C. Barnes, “An energy- and charge-conserving, implicit, electrostatic particle-in-cell algorithm,” *Journal of Computational Physics*, vol. 230, pp. 7018–7036, 2011.
- [8] S. Markidis and G. Lapenta, “The energy conserving particle-in-cell method,” *Journal of Computational Physics*, vol. 230, no. 18, pp. 7037–7052, 2011.
- [9] W. T. Taitano, D. A. Knoll, L. Chacón, and G. Chen, “Development of a consistent and stable fully implicit moment method for Vlasov-Ampère Particle-in-cell (PIC) system,” *SIAM J. Sci. Comput.*, vol. 35, no. 5, pp. S126–S149, 2013.
- [10] G. Chen and L. Chacón, “An energy- and charge-conserving, nonlinearly implicit, electromagnetic 1D-3V Vlasov-Darwin particle-in-cell algorithm,” *Comput. Phys. Commun.*, vol. 185, no. 10, pp. 2391–2402, 2014.
- [11] G. Chen and L. Chacón, “A multi-dimensional, energy- and charge-conserving, nonlinearly implicit, electromagnetic vlasov-darwin particle-in-cell algorithm,” *Comput. Phys. Commun.*, vol. 197, pp. 73–87, 2015.
- [12] D. A. Knoll and D. E. Keyes, “Jacobian-free Newton-Krylov methods: a survey of approaches and applications,” *J. Comput. Phys.*, vol. 193, no. 2, pp. 357–97, 2004.
- [13] H. F. Walker and P. Ni, “Anderson acceleration for fixed-point iterations,” *SIAM Journal on Numerical Analysis*, vol. 49, no. 4, pp. 1715–1735, 2011.
- [14] A. B. Langdon, ““Energy conserving” plasma simulation algorithms,” *J. Comput. Phys.*, vol. 12, pp. 247–268, 1973.
- [15] H. R. Lewis, “Energy-Conserving Numerical Approximations for Vlasov Plasmas,” *Journal of Computational Physics*, vol. 6, pp. 136–141, 1970.
- [16] G. Lapenta, “Exactly energy conserving semi-implicit particle in cell formulation,” *Journal of Computational Physics*, vol. 334, pp. 349–366, 2017.

- [17] L. Chacón, G. Chen, and D. C. Barnes, “A charge- and energy-conserving implicit, electrostatic particle-in-cell algorithm on mapped computational meshes,” *Journal of Computational Physics*, vol. 233, pp. 1–9, 2013.
- [18] A. Hindmarsh, “Lsode and lsodi, two new initial value ordinary differential equation solvers,” *ACM SIGNUM Newsletter*, vol. 15, pp. 10–11, 1980.
- [19] D. A. Bini, “Numerical computation of polynomial zeros by means of Aberth’s method,” *Numerical algorithms*, vol. 13, no. 2, pp. 179–200, 1996.
- [20] J. Brackbill and D. Forslund, “An implicit method for electromagnetic plasma simulation in two dimensions,” *Journal of Computational Physics*, vol. 46, p. 271, 1982.